

Droplet epitaxy InAs/InP quantum dots in etched pits for single photon emitters at 1550 nm: morphology, optical and electronic properties, and etching kinetics

Paweł Holewa^{1,2*}, Shima Kadkhodazadeh^{3,4}, Michał Gawęlczyk^{5,*}, Paweł Baluta², Vladimir G. Dubrovskii⁶, Marcin Syperek², Elizaveta Semenova^{1,4}

1 DTU Fotonik, Technical University of Denmark, Kongens Lyngby DK-2800, Denmark

2 Laboratory for Optical Spectroscopy of Nanostructures Department of Experimental Physics, Faculty of Fundamental Problems of Technology, Wrocław University of Science and Technology, Wybrzeże Wyspiańskiego 27, 50-370 Wrocław, Poland

3 DTU Nanolab–National Centre for Nano Fabrication and Characterization, Technical University of Denmark, Kongens Lyngby DK-2800, Denmark

4 NanoPhoton-Center for Nanophotonics, Technical University of Denmark, DK-2800 Kongens Lyngby, Denmark

5 Department of Theoretical Physics, Faculty of Fundamental Problems of Technology, Wrocław University of Science and Technology, 50-370 Wrocław, Poland

6 Faculty of Physics, St. Petersburg State University, Universitetskaya Embankment 13B, 199034, St. Petersburg, Russia

* Currently at: Institute of Physics, Faculty of Physics, Astronomy and Informatics, Nicolaus Copernicus University, Toruń 87-100, Poland.

KEYWORDS Quantum Dots, Epitaxy, STEM, Single-Photon Sources

Abstract

We utilize a droplet epitaxy scheme to fabricate low surface density ($2.8 \times 10^8 \text{ cm}^{-2}$) InAs quantum dots on an (001)InP substrate with nearly symmetric quantum confinement potential, emitting at the third telecom window. We show that the local etching of the In droplet results in the formation of nearly-symmetric QDs with an arch-shaped base and we explain the QD growth kinetics by the atom diffusion model. Electronic band structure calculations reveal properties of neutral and charged excitons confined in the dots, including respective emission and binding energies. These values are confirmed in the high-spatially-resolved photoluminescence experiment. We show that the quantum dots can be considered as non-classical photon emitters with a high single-photon emission purity at $\sim 1500 \text{ nm}$.

1. Introduction

Epitaxially-grown semiconductor quantum dots (QDs), among other solutions, are considered as nearly perfect quantum emitters^{1,2} with many applications in quantum communication³ and quantum computation^{4,5} technologies. QDs emitting in the long-wavelength third telecom band centered at 1550 nm are of special interest for these applications. They offer ultra-low-loss single-photon-encoded data transmission between quantum nodes both in distributed silica-fiber-based optical networks⁶ and on-chip silica waveguides⁷.

Two main material systems are employed to fabricate the long-wavelength single-photon emitters: InAs/GaAs^{8–11} and InAs/InP^{12–14}. GaAs-based QDs show excellent single-photon emission properties¹⁵, including high single-photon emission purity^{9,11}, and the degree of photon indistinguishability¹⁰, but at

the cost of complicated fabrication technology (strain engineering), necessary to red-shift the emission wavelength^{16,17}. In comparison, InP-based QDs naturally emit at longer wavelengths, offering high photon emission purity^{12,17} and indistinguishability¹⁸. However, controlling the growth kinetics and the morphology of the resulting InAs/InP QDs is complicated regarding, e. g., size, shape anisotropy, and areal density of QDs. Therefore, establishing an optimal fabrication scheme will make the InAs/InP QDs a highly competitive solution for solid-state single-photon quantum emitters in the long-wavelength telecom range.

Up till now, two main growth schemes have been utilized in the epitaxy of InAs/InP QDs with the demonstration of single-photon emission in this material system: (i) Stranski-Krastanov (SK) growth mode^{12,19}, and (ii) droplet epitaxy (DE)^{13,14,20}. SK InAs/InP QDs hold the record for single-photon generation purity at the long-wavelength spectral range¹². DE InAs/InP QDs quickly followed the entangled photon pairs emission²¹, hardly accessible for the SK counterparts. DE QDs are appealing as their growth is not strain-driven, is more controllable, and is compatible with site-selective QD nucleation compared to SK QDs²⁰. Additionally, DE QDs are typically more symmetric compared with the SK QDs¹³.

The high symmetry of QD confining potential is important for the effective generation of entangled photon pairs due to the direct influence on the exciton fine structure splitting (FSS) energy¹. The symmetry is, however, often inherited from the substrate: employing the high-Miller index planes, such as (111)A-²² and (111)B-oriented GaAs²³ or InP(111)A substrate with C_{3v} symmetry^{24,25}, is a common but impractical solution. Additionally, this route initially considered very promising²⁶, often results in the average FSS values of $(60 \pm 38 \text{ } \mu\text{eV})$ ²⁷, clearly questioning this picture. Therefore, it is appealing to modify the DE route by applying the local droplet etching (LDE) known from the GaAs-based QDs^{28,29}. Within the LDE approach, the QD nucleation sites are created by the surface etching of symmetric metallic droplets. QDs fabricated by the nanohole filling have the symmetry forced by the nanohole and hence have very low FSS values, including structures grown on industry-compatible (001) substrates^{30,31}, demonstrating the quantum communication schemes based on the entangled photon pairs³.

However, changing the (001)GaAs substrate to (001)InP leads to different results. As recently shown by Sala *et al.*³², applying the droplet etching in the InP system results in local etching of asymmetric pits around the QDs instead of the QDs themselves. Here, we show the advantages of this new epitaxial scheme by comparing the same QDs with and without etching and find that this approach is promising for reaching the 1.55 μm emission with low-density DE QDs and to simultaneously increase their symmetry.

In this work, we present a detailed investigation of morphology, chemical composition, electronic structure and optical properties of individual InAs/InP QDs of low surface density ($2.8 \times 10^8 \text{ cm}^{-2}$), grown by droplet epitaxy, and emitting at the 3rd telecom window, covering the S- (1460-1530 nm), C- (1530-1565 nm), and L- (1565-1625 nm) bands. We explain the formation of asymmetric pits, in which the QDs are finally positioned. The shape and composition of buried QDs are studied by high-resolution scanning transmission microscopy (HR STEM) and energy dispersive X-ray spectroscopy (EDX). The QDs are surrounded by a 2D layer similar to the wetting layer inherent to SK growth mode of self-assembled QDs. However, the nature of this layer is different and its origin is explained based on the kinetic theory of nucleation and anisotropic diffusivity of indium atoms. Theoretical calculations, done using the 8-band $k \cdot p$ and configuration-interaction methods and based on our morphological investigations, support the optical properties of individual QDs measured by the low-temperature

photoluminescence (PL). Due to the low density of the QDs, we perform the micro-PL (μ PL, also time-resolved) studies of excitonic complexes on a single QD. The single lines show large activation energy for the temperature-induced quenching of the PL, (74 ± 13 meV), promising for non-classical light sources used at elevated temperatures, and PL decay time of ~ 1.7 ns. We show that the fabricated QDs are good candidates for single-photon sources emitting at $1.55 \mu\text{m}$ by presenting the high purity of single-photon emission with the as-measured value of 92.5% and fitted $g^{(2)}_{\text{fit}}(0) = 0$ with the standard error of fitting procedure $\sigma = 0.11$.

The samples under investigation contain two QD arrays grown under the same conditions by low-pressure metalorganic vapor phase epitaxy (MOVPE) on (001)-oriented InP substrate. The first array is covered by an InP matrix (these QDs are optically active), and the second QD layer is left uncovered on the InP surface for the atomic force microscopy (AFM) investigation. The procedure of QD synthesis includes two steps. First, In droplets are formed by depositing trimethylindium (TMIn) in the absence of Vth group atoms on the InP surface at 360°C , followed by 60 s long waiting time. Afterwards, In droplets are annealed under arsine (AsH_3) ambient (the temperature rises up to 550°C for 130 s, followed by 180 s annealing under arsine ambient) before the overgrowth by the InP cap layer. For the reference structure without annealing, the temperature after the 60 s long waiting time is raised to 475°C for 70 s with immediate InP layer deposition. A detailed description of the growth procedure can be found in the Methods section.

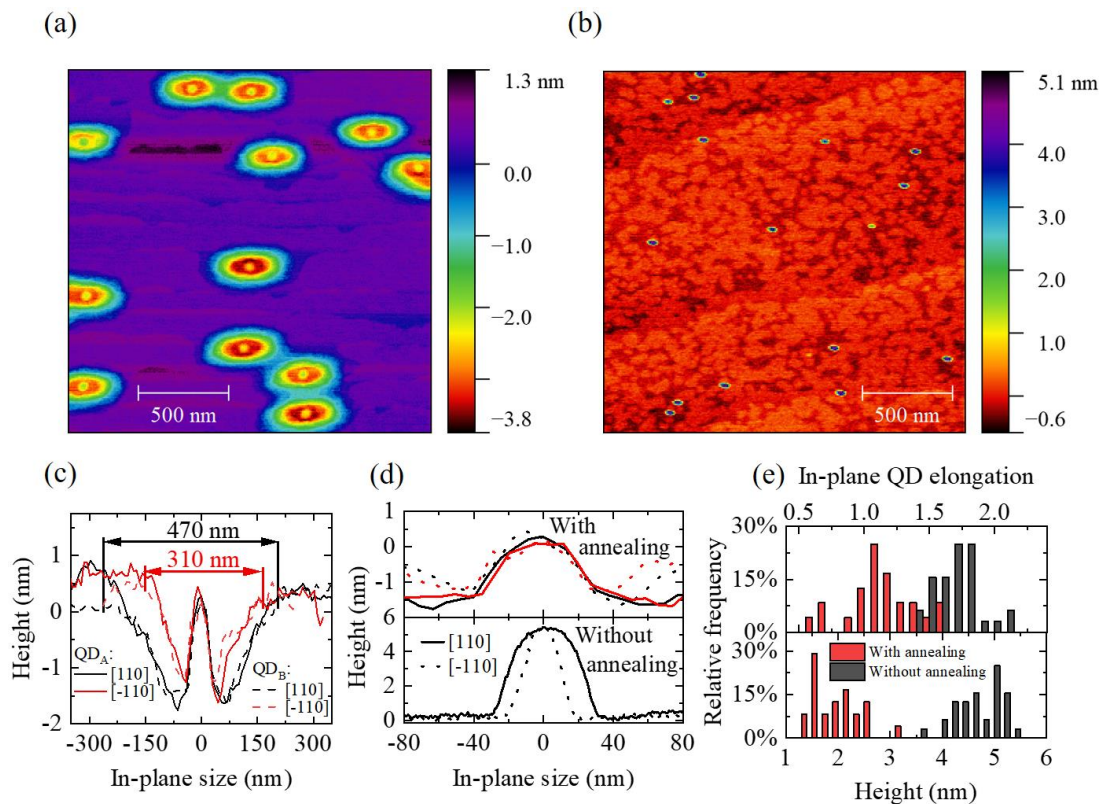


Figure 1. Morphological investigation of surface DE QDs by atomic force microscopy, (2×2) μm^2 scans. (a) Annealed QDs in etched pits. (b) QDs before annealing. (c) Cross-section scans of the pits around annealed QDs. (d) Comparison of the QD cross-sections: after annealing [top panel, close-up of (c)] and before annealing (bottom). (e) Statistics of the QD in-plane elongation (top) and height (bottom).

2. Results

2. 1. Structural investigations

The QDs morphology was first investigated by AFM. Figure 1(a) presents a typical AFM image for the surface QDs after annealing. First, it revealed a low QDs surface density of roughly $2.8 \times 10^8 \text{ cm}^{-2}$, comparable to the QDs without annealing, displayed in Fig. 1(b). Second, every annealed QD is located in a dip formed by local etching of the InP material around the In droplet³². Figure 1(c) shows exemplary cross-sectional profiles of the AFM scans at the places with QDs, revealing the pit's shape. The pits are asymmetric, with typical width of $\sim 470 \text{ nm}$ along the [110] direction and $\sim 310 \text{ nm}$ along [-110]. The high-resolution QD AFM profiles evidence the high symmetry of annealed QDs (top panel) regarding the unannealed counterpart (bottom panel). This observation is confirmed by statistical analysis of the dot profiles presented in Fig. 1(e), showing that the in-plane aspect ratio for annealed QDs, defined as the ratio of the QD base median length along [110] and [-110] directions is 1.09 for annealed QDs and 1.75 for the unannealed dots. We also observe a severe lowering of the height of surface QD by annealing, from $H \approx 4.8 \text{ nm}$ to $H \approx 1.9 \text{ nm}$ [bottom panel in Fig. 1(e)]. For the annealed QDs, we define H as the height of a QD measured from the bottom of the pit to the QD apex.

We observe new details about the shape of buried QDs by examining them in cross-section using high resolution scanning transmission microscope image (HR STEM)³³ and energy-dispersive x-ray spectrometry (EDX). The results are summarized in Figure 2, where we show cross-sections of QDs viewed along the [-110] (top row) and [110] directions (middle row), and on the 2D layer (bottom row). Figs. 2(a) and 2(b) present HR STEM images of annealed QDs in cross-section. While the base length is kept unchanged (in a range of measurement error and a size distribution), the height of the buried QDs is higher. They appear as truncated pyramids with arched bottom bases and with symmetric in-plane dimensions. They have a bottom base length of $B = (45 \pm 2) \text{ nm}$, top length of $T = (33 \pm 1.7) \text{ nm}$ and height of $H = (5.2 \pm 0.3) \text{ nm}$. The chemical composition of these QDs is found to be $\text{InAs}_x\text{P}_{1-x}$ with $x = 80\% \pm 15\%$, measured both by EDX and by analyzing the change in the lattice parameter along the [001] direction from the atomic resolution STEM images (for details, see Methods). The color-coded maps of changes in the [002] lattice spacing relative to the InP substrate (e_{yy}) are shown in Fig. 2(d)-(f). Line scans of e_{yy} across the QDs and As and P composition profiles obtained from EDX measurements are plotted in Fig. 2(g)-(i). Additional EDX data is shown in Supplementary Figure 1. The 2D layer is 2-3 ML thick and has a composition of $\text{InAs}_x\text{P}_{1-x}$ with $x = 50\% \pm 15\%$. Moreover, we consistently observe a region above the 2D layer containing up to 20% As and extending to around 15 nm above it.

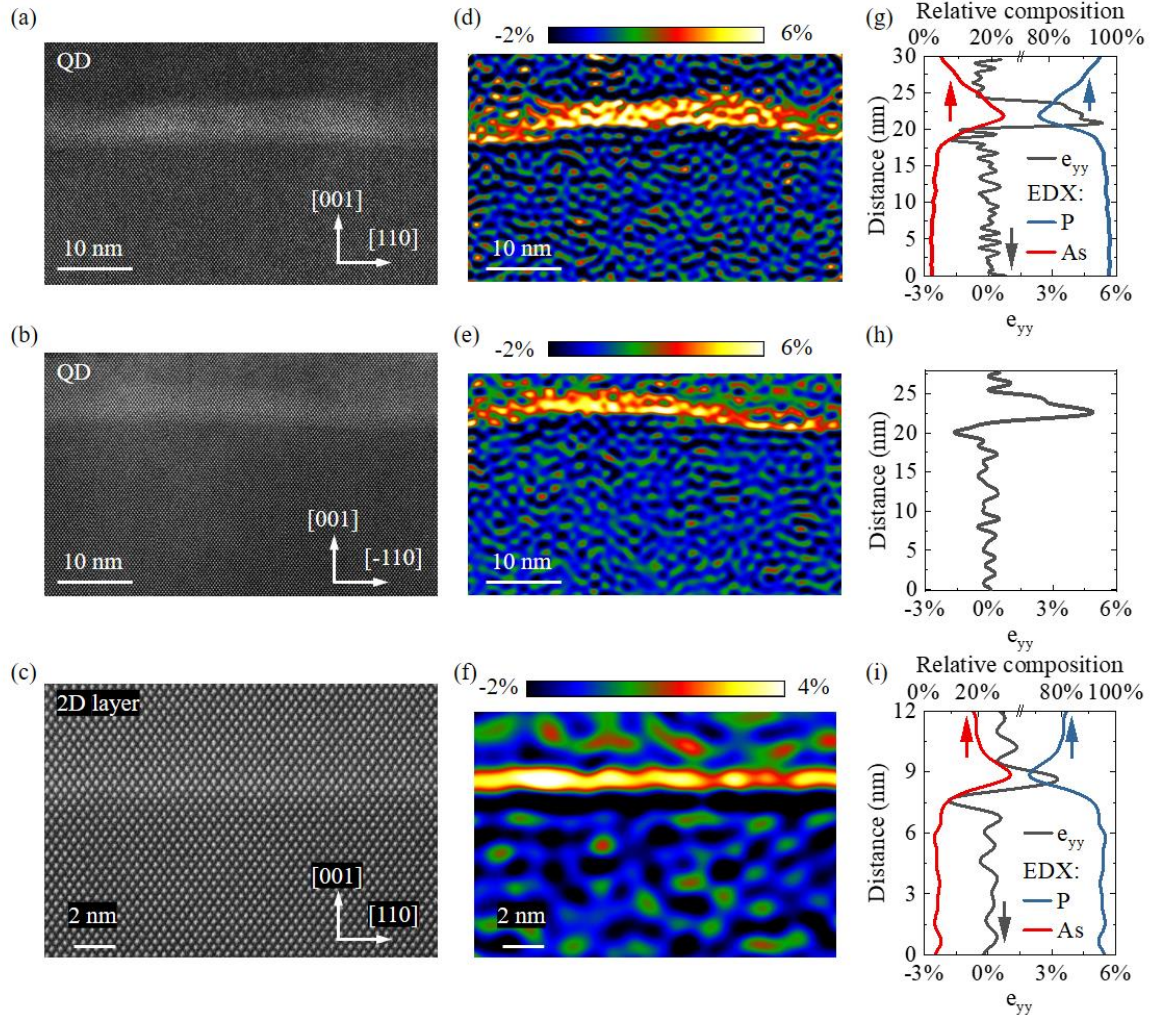


Figure 2. Morphological investigation of the buried DE QDs in HR STEM and EDX. QDs in cross-section geometry viewed along the (a) [-110] and (b) [110] directions and (c) the 2D InAsP layer. (d)-(f) Maps representing the fractional change in the [002] lattice spacing (relative to the InP lattice), e_{yy} , for each of the images in a-c. (g)-(i) Line scan profiles of P (blue) and As (red) concentrations measured by EDX, and the lattice displacement values e_{yy} (black lines) along the [001] direction.

Compared to SK QDs, DE QDs are without a wetting layer due to the very different nature of their nucleation¹³. For the commonly studied InAs/GaAs QDs, the dot and the barrier share the Vth group atoms, while in the case of our studied InAs/InP QDs, the group Vth atoms are switched at the QD interface. This occurs during the exposure of the InP surface to the AsH₃ ambient in the QD crystallization step. As the Vth group ions are volatile, P atoms desorbing from the surface are substituted by As atoms, forming a 2D layer of InAs_xP_{1-x}^{34,35}. The thickness h of this 2D layer is $h \approx 3$ MLs, as estimated from the HR STEM images [Fig. 2(i)]. The chemical composition is estimated from the lattice displacement in [001] direction, as shown by the colored map in Fig. 2(f) and the profiles in Fig. 2(i). For EDX data of the 2D layer, see Supplementary Figure 2.

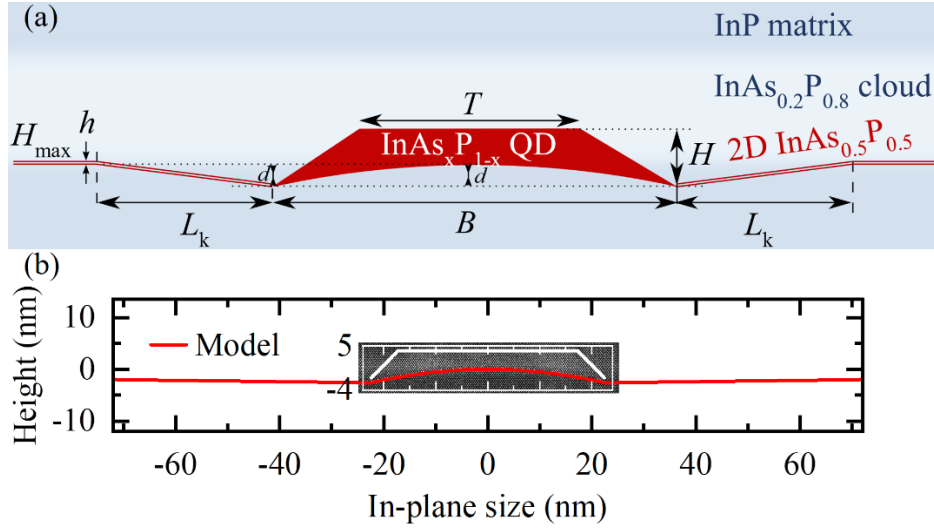


Figure 3. (a) Model of a QD and surrounding pit inferred from the STEM scans. (b) The modelled profile of the bottom plane of the QD and the 2D layer surrounding it (red line) overlaid on the STEM image in Fig. 2a. The white line indicates the QD top plane.

Combining the structural data presented in Fig. 1 and Fig. 2, we construct a model for buried QDs, formed in etched pits, and surrounded by an InAsP material cloud. The model is presented in Fig. 3(a). In the following part of the article, we focus our description on a symmetric QD with dimensions inferred from the STEM measurements (“QD1”). For such a QD we assume in-plane bottom base length of $B = 43$ nm and top length of $T = 33$ nm. Secondly, we consider also the modified in-plane dimensions of a QD to account for the QD elongation of 1.09, as measured in AFM for surface QDs. Then, we resize the dimensions to $B = 41.1$ nm and $T = 31.6$ nm along the $[-110]$ direction, and $B = 44.9$ nm and $T = 34.4$ nm along the $[110]$ direction (“QD2”).

Interestingly, STEM images show that the bottom base of the QD is arched upwards, where the sides are at the same level as the etched pits around the QDs and the middle is approximately at the same level as the substrate outside the pits. Therefore, in our model we keep the pit’s depth and the material underneath the QD equal [marked with d in Fig. 3(a)]. For QD1 we take $d = 1.9$ nm in both directions, and for QD2 $d = 2.6$ and $d = 2$ nm along the $[110]$ and $[-110]$ directions. For both QDs we keep the same in-plane distance L_k between the QD base and the substrate outside the pit: $L_k = 213$ nm along $[110]$ and $L_k = 133$ nm along the $[-110]$ direction.

2. 2. Formation of pits around QDs

In modeling, we try to understand the unusual process of forming the pits around DE QDs in the 3 min annealing stage at 550 °C. Annealing takes place under As flux, while P is available in the InP substrate. We need, however, an In supply to form additional InAsP material in the island during annealing, most probably followed by In evaporation (leading to the observed decrease in the height of the annealed QDs). According to Refs.^{36,37}, In incorporation occurs preferentially through the perimeter of the island base in contact with 2D InGaAs layer, where the elastic stress induced by the lattice mismatch is highest. Coordinate-dependent coverage of the substrate with 2D layer θ can be described using the steady-state diffusion equation

$$\frac{d^2\theta}{dx^2} = -I_k\Omega/(D_k h). \quad (1)$$

Here, x is the coordinate along a given crystallographic direction (either [-110] or [110]), Ω is the elementary volume per one III-V pair, h is the height of InAsP monolayer (ML), I_0 and D_0 are the In flux ($\text{nm}^{-2}\text{s}^{-1}$) and diffusion coefficient for In solid diffusion from the substrate to 2D layer around the island, while I_1 and D_1 describe In diffusion from the substrate into the island through the interface beneath the QD. The diffusion process is driven by the elastic stress field, as in Ref. ^{36,37}, which depends on the position of the 2D layer around or beneath the island.

The relevant boundary conditions are given by

$$\theta(x = L) = \theta_{\min}, \theta(x = L + \lambda) = \theta_{\max} \text{ for } L \leq x \leq L + \lambda, \quad (2)$$

and

$$\left(\frac{d\theta}{dx}\right)_{x=0} = 0, \theta(x = L) = \theta_{\min} \text{ for } 0 \leq x \leq L. \quad (3)$$

The height profile of 2D layer is then obtained as $H - H_{\max} = -I_k\Omega t(\theta_{\max} - \theta)$, with H_{\max} as the height outside the pit (the zero level) and t as the annealing time. According to Eq. (2), the 2D layer thickness is minimum at the island boundary (with L as a half of the island width along a given direction) and zero outside the pit (with λ as the effective diffusion length of In atoms in this direction). According to Eq. (3), the 2D layer thickness reaches its maximum at $x = 0$ by symmetry. Our measurements show that this maximum is very close to zero, meaning that etching of the 2D layer is negligible in the center of the pit.

Solutions for the pit cross-sections along the [-110] and [110] directions are given by

$$H - H_{\max} = -I_0\Omega\Delta\theta t \left[1 - \frac{x-L}{\lambda} - \frac{(2L+\lambda)(x-L)+L^2-x^2}{r_0^2} \right], L \leq x \leq L + \lambda \quad (4)$$

around the QD and

$$H - H_{\max} = -I_1\Omega\Delta\theta t \left[1 - \frac{L^2-x^2}{r_1^2} \right], 0 \leq x \leq L \quad (5)$$

beneath the QD, with $r_0^2 = 2D_0h\Delta\theta/(I_0\Omega)$, $r_1^2 = 2D_1h\Delta\theta/(I_1\Omega)$, and $\Delta\theta = \theta_{\max} - \theta_{\min}$. According to our data, the height profiles of the pits around the QD are linear within the AFM experimental

accuracy (the slope d/L_k is only 1-2%), corresponding to $r_0 \rightarrow \infty$ in Eq. (4). This should be due to a high diffusivity of In in 2D layer relative to the diffusivity of In at the island-substrate interface ($D_0 \gg D_1$). Lines in Supplementary Figure 3 show the excellent fits to the measured cross-sections of the pits around symmetric QD1 and asymmetric QD2, as well as the dome-shaped cross sections beneath the QDs. The fits are obtained with $I_0\Omega\Delta\theta t = I_1\Omega\Delta\theta t = 1.9$ nm, $L = 21.5$ nm, $r_1 = 21.5$ nm, $\lambda = 132.5$ nm in the [-110] direction and 213 nm in the [110] direction for symmetric QD1. For asymmetric QD2, we use the same λ , $I_0\Omega\Delta\theta t = I_1\Omega\Delta\theta t = 2.0$ nm, $L = 20.56$ nm, $r_1 = 20.58$ nm in the [-110] direction, and $I_0\Omega\Delta\theta t = I_1\Omega\Delta\theta t = 2.6$ nm, $L = 22.44$ nm and $r_1 = 22.4$ nm in the [110] direction. In all cases, the values of r_1 are very close to L , which is required to disable etching in the center of the pit. The fitting values of $I_0\Omega\Delta\theta t$ and $I_1\Omega\Delta\theta t$ appear identical, showing that the supply of In is the same around and underneath the QDs, while different shapes of the cross sections are due to different diffusion coefficients of In atoms. The effective diffusion length of In atoms is larger along the [110] direction. Fitting the asymmetric pit profiles requires that the etching process occurs at different rates along the two directions.

2. 3. Electronic and optical properties of individual QDs

The broadband optical response of the ensemble of QDs is shown in Fig. 4(a), and it covers the whole 3rd optical-fibre window and a range of shorter wavelengths. The emission energy for the annealed QDs is significantly red-shifted compared to the QDs without annealing (emitting at ~ 1220 nm). See Supplementary Figure 4 for the PL data of the QDs without annealing. At this point, we may check whether our model of a reference QD based on morphological data and presented in Fig. 3(a) reproduces the observed emission energy. To this end, we calculate the electron and hole eigenstates within the multiband envelope-function $k\cdot p$ theory, and next, within the configuration-interaction approach, we find the states of various carrier complexes: neutral excitons (X), charged excitons (X^- , X^+), and biexcitons (XX). Details of numerical calculation and parameters used are given in Methods.

We probe a range of parameters around those found from morphological studies, i. e., $x = 80$ % and $H = 5.4$ nm, to see how their variation affects experimentally accessible QD optical properties. Here, H is defined along the [-110] direction. Calculated X ground-state energy for a series of calculations with $x = 72\%$ - 88% and H varied between 3.6 and 6.0 nm, is presented with points against the PL spectrum in Fig. 4(a). The range of calculated energies covers the width of the measured spectrum, while the reference parameters give $E_X \sim 0.82$ eV, which is close to the median of the PL band. This agreement supports our QD model based on morphological studies.

To repetitively address a pre-selected single QD, we produce an array of micro-pillar-like round mesas with the diameter of (0.2-3) μm . For the largest mesas, the diameter of the diffraction-limited laser spot in the μPL experiment is smaller than the mesa size, which means that the restricting role of the mesa is greatly reduced in this case. An exemplary μPL spectrum for a large mesa (2.9 μm) is presented in Fig. 4(a). The spectrum covers S-, C-, and L-bands and shows a handful of well-isolated emission lines, evidencing the presence of only a few optically active QDs within the excitation spot.

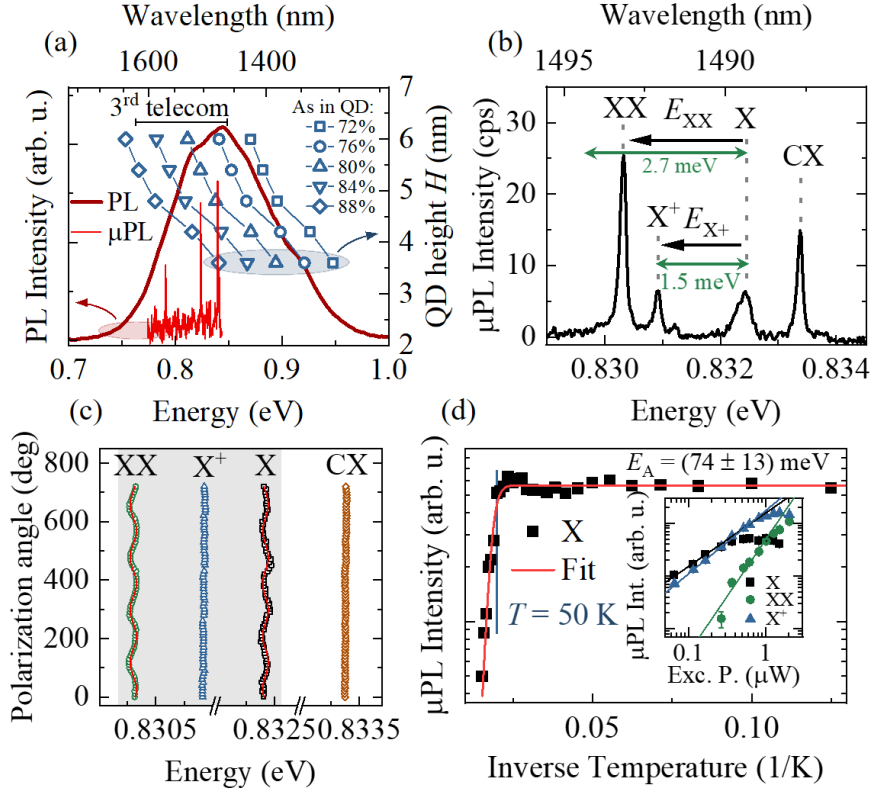


Figure 4. (a) Low-temperature ($T = 10$ K) PL spectrum of annealed QDs overlapped with the μ PL spectrum ($T = 4.2$ K) from a large mesa, showing well-resolved single emission lines. Right axis: calculated emission energies as a function of QD height and As content in the QD. (b) μ PL spectrum of an individual QD with identified excitonic complexes (exciton, X, positive trion, X^+ , and biexciton, XX), as well as a trion line from a neighboring QD (CX). (c) Polarization-resolved μ PL for the lines shown in panel (b). (d) Temperature dependence of the X line μ PL intensity with the Arrhenius fit line. Inset: Power dependence of the μ PL intensity for excitonic complexes in the identified QD.

The exemplary μ PL spectrum of a single QD emitting in the S-band is presented in Fig. 4(b). The energies of the excitonic complexes form a pattern with a trion binding energy ~ 1.5 meV and ~ 2.1 meV for the biexciton. Another charged exciton (CX) line (observable at emission energy higher than X) originates from a neighboring QD (we exclude the negative trion, based on the theoretical calculations). The identification of excitonic complexes is in agreement with the excitation-power-dependent series, with the line's intensity I plotted as a function of the excitation power P in the inset of Fig. 4(d). The exciton has a linear power dependence ($I_X \sim P^{1.01}$), biexciton - quadratic ($I_X \sim P^{1.95}$), and positive trion - superlinear ($I_{X^+} \sim P^{1.20}$), as expected^{38,39}. The polarization-resolved μ PL shows anti-phase energy oscillations of XX-X emission lines, while the X^+ and CX lines show no polarization dependence, which further strengthens the identification of the lines. The exciton fine structure splitting is $\sim (50 \pm 5)$ μ eV, evidencing a minor QD of confining potential in accordance with the almost symmetric shape of QDs. The anisotropy and disorder on the atomic level of the QD chemical composition, strain and electric fields in the vicinity of the QD are among the sources of the observed splitting.

We turn to theoretical model again, and calculate the eigenstates of carrier complexes and their optical properties for the reference QD2 and for its idealized version, QD1, lacking the minor deviations from

the perfect symmetry (small elongation and difference in bottom arc for the two cross sections), to see how these small deviations impact the relevant properties. The results are summarized in Table I.

Table I. Results of calculation for the idealized (QD1) and reference (QD2) models of a QD: first excited level splitting for the electron and the hole, light-hole admixture, X ground state energy, degree of linear polarization (DOP), X lifetime, carrier-complex binding energies.

	e_2-e_1 (meV)	h_2-h_1 (meV)	lh admix. (%)	E_X (meV)	DOP (%)	τ_X (ns)	Δ_{X^-} (meV)	Δ_{X^+} (meV)	Δ_{XX} (meV)
QD1	10.18	7.64	0.056	823.82	0.32	0.87	3.01	1.64	2.78
QD2	7.60	7.77	0.06	818.75	1.42	0.84	2.99	1.43	2.63

Based on matching of calculated binding energies, we confirm the assignment of the lower-energy trion line as X^+ from the given QD, and the other CX line as coming from a different QD, as the theoretically expected binding energy for X^- is far different. The calculated splittings are marked in Fig. 4(b) with green arrows for comparison.

We note here also that the minor deviations from rotational symmetry found in the QD morphology translate, according to theoretical results, into insignificant variation of relevant optical properties, apart from discussed emission and binding energies including also negligible light-hole admixture to the hole ground state (main source of large FSS in QDs⁴⁰) and the DOP.

The temperature-dependent μ PL intensity for the exciton line is investigated to evaluate the prospects for single-photon applications at elevated temperatures, such as Stirling-compatible cryocooler⁴¹. The quenching of the μ PL intensity is observable at temperatures relatively high as for the pure InP barriers, starting from $T = 50$ K. The quenching of the integrated μ PL intensity is fitted with the standard formula with a single activation processes:

$$I(T) = I_0/[1 + B\exp(-E_A/k_B T)], \quad (6)$$

where I_0 is the μ PL intensity for $T \rightarrow 0$, E_A is the activation energy, and B is the quenching rate. We obtain the activation energy $E_A = (74 \pm 13)$ meV, which is much larger than ~ 20 meV, typically observed for SK InAs/InP QDs⁴² or InAs/InAlGaAs quantum dashes⁴³ where the presence of the wetting layer is often detrimental for the high-temperature stability of single-photon emission.

The purity of single-photon emission of the QDs is investigated by performing the autocorrelation spectroscopy of the CX line [shown in Fig. 4(b)]. We choose the charged exciton due to its high intensity and perform the Hanbury Brown and Twiss interferometry to obtain the second-order autocorrelation function $g^{(2)}(\tau)$, where τ is the time delay between consecutive detected photons. Its value at $\tau = 0$ evaluates the purity of single-photon emission. The normalized histogram of coincidences, plotted in Fig. 5(a), is fitted with the standard function⁴⁴:

$$g^{(2)}(\tau) = 1 - [1 - g_{fit}^{(2)}(0)]\exp(-|\tau|/t_r), \quad (7)$$

where $g_{fit}^{(2)}(0)$ is the single-photon emission purity, and $t_r = 1/(\Gamma + W_p)$ is the antibunching time constant with Γ being the electron-hole radiative recombination rate, and W_p - the effective pump rate. We obtain the as-measured value of $g_{meas}^{(2)}(0) = 0.075$ and $g_{fit}^{(2)}(0) = 0$ with the standard error of fitting procedure $\sigma = 0.11$ (without any background correction or other data post-processing) and $t_r = (0.58 \pm 0.09)$ ns. The obtained low value of $g_{fit}^{(2)}(0)$ proves high purity of single-photon emission, showing the potential of the investigated QDs in quantum information processing as single-photon emitters at third telecom window.

Finally, we investigate the CX decay rate in the time-resolved μ PL experiment [Fig. 5(c)]. The PL decay time for the investigated line is $\tau_{CX} = (1.72 \pm 0.02)$ ns, obtained from the fitting of the monoexponential decay [$I(t) \sim I(0)\exp(-t/\tau)$] to the data and suggesting the considerable contribution of the effective pump rate to lowering the t_r . The obtained τ_{CX} is within the range of experimentally obtained values for excitonic complexes confined in InAs/InP QDs^{18,19,45} or InAs/InAlGaAs/InP QDs⁴⁶.

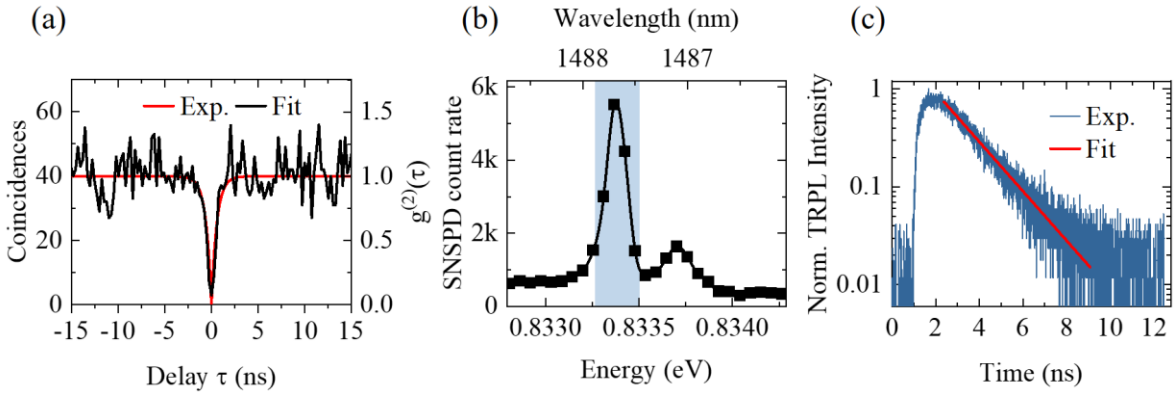


Figure 5. (a) Autocorrelation histogram for the CX line with (b) the corresponding μ PL spectrum recorded on superconducting nanowire single-photon detectors. Shaded area marks the monochromator band-pass. (c) Time-resolved photoluminescence for the CX line with the monoexponential fit line.

3. Summary

In summary, we have fabricated low-surface density InAs QDs on a (001)InP substrate, utilizing the droplet epitaxy scheme in the molecular-vapour phase reactor. By employing the local In droplet etching step, the dots are effectively symmetrized, localized in asymmetric pits and emit at third telecom window. The QD shape morphology is investigated by atomic force microscopy and high-resolution scanning transmission electron microscopy. The pit etching is explained through the atom diffusion model. The electronic properties of the dots are predicted by the numerical calculations within the 8-band $k \cdot p$ framework. The theory shows the expected range of energies for the neutral exciton, and binding energies for the biexciton and charged exciton complexes confined in the nearly symmetric potential of a quantum dot. The optical properties of QDs are examined in the high-spatially-resolved photoluminescence experiment and agree well with the theoretical expectations. Finally, QDs show excellent single-photon emission properties: the Hanbury-Brown and Twiss-type interferometric

experiment on a charged exciton emission complex has revealed nearly 93% of single-photon emission purity at ~1500 nm, showing that these dots are interesting candidates for single-photon emitters at the telecom spectral range.

Methods

QD nucleation. The QDs are grown in the low-pressure MOVPE TurboDisc[®] reactor using arsine (AsH₃), phosphine (PH₃), tertiarybutylphosphine (TBP) and trimethylindium (TMIn) precursors with H₂ as a carrier gas. The growth sequence starts with a 0.5 μm-thick InP buffer layer deposition on an (001)-oriented InP substrate at 610°C. Then, the temperature is decreased to 360 °C and stabilized under TBP first. The deposition of indium droplets occurs under the TMIn flow rate of 13 μmol/min with nominally 1.8 ML-thick indium layer. The indium droplets are annealed for 60 s and the temperature is being raised for 130 s to 550 °C under AsH₃ with the flow rate of 52.2 μmol/min. Afterwards, we keep the temperature constant for 180 s and deposit the 30 nm-thick InP. Finally, we repeat the indium deposition and annealing for the surface QDs. For the reference structure without annealing, the temperature after the 60-s long waiting time is raised to 475 °C for 70 s followed by the immediate InP layer deposition and the sequence of surface QDs finishes the structure.

Scanning transmission electron microscopy. Electron transparent lamellas of the cross-sections of the samples were prepared by focused ion beam milling (FIB) using a Helios Nanolab dual beam instrument. The FIB milling and polishing was carried out using a Ga⁺ beam at 30kV and with currents ranging from 2nA - 20pA. The samples were then further polished in an Ar⁺ Nanomill instrument at 700V in order to remove FIB induced damage. High-angle annular dark-field STEM images of the samples were acquired using a FEI Titan 80-300 instrument fitted with a field emission gun and with an aberration-corrector on the probe forming lenses, operated at 300 kV. The electron probe had a convergence semi-angle of 18 mrad and the images were recorded on an annular detector with an inner collection semi-angle of 50 mrad. Geometric phase analysis was applied to the images to obtain lattice displacement maps along the [001] direction using the freely available FRWRtools script (<https://www.physics.hu-berlin.de/en/sem/software>). The obtained changes in the lattice spacing along the growth direction and the Poisson ratio of InAs were then used to estimate the As content of the examined regions.

Optical experiments. During the optical experiments, the structure is held in a helium-flow cryostat allowing for the sample's temperature control in the range of 4.2-300 K. For the μPL studies, structures are excited by a 640 nm line from a cw semiconductor laser diode through a high-numerical (NA = 0.4) microscope objective with 20-times magnification. The same objective is used to collect the μPL signal and to direct it for the spectral analysis with a 1 m-focal-length monochromator equipped with a liquid-nitrogen-cooled InGaAs multichannel array detector, providing spatial and spectral resolution of ~2 μm and on the order of 25 μeV, respectively. Polarization properties of emitted light are analyzed by rotating the half-wave retarder mounted before a fixed high-contrast-ratio (10⁶:1) linear polarizer placed in front of the monochromator's entrance.

Autocorrelation histograms and TRPL are measured in a similar setup. However, the structure is excited by a 787 nm cw laser line for correlation spectroscopy, and by a train of ~50 ps-long pulses at the frequency of 80 MHz, and the central photon wavelength of 805 nm. In this case, the collected photons are dispersed by a 0.3 m-focal-length monochromator equipped either by the InGaAs multichannel array detector or the NbN-based superconducting nanowire single-photon detectors with ~90% efficiency in the 1.5-1.6 μm range and ~200 dark counts per second. A multichannel picosecond event timer analyzes

the single photon counts as the time-to-amplitude converter with the 256 ps channel time bin width. The overall time resolution of the setup is ~ 80 ps.

8-band $k\cdot p$ calculations. The material composition profiles of simulated QDs, as presented in Fig. 3(a), are discretized and represented on a numerical grid. The lattice mismatch between the constituent materials leads to a strain field, which is calculated within the standard continuum elasticity theory, such that it minimizes the total elastic energy of the system. As the materials are noncentrosymmetric, the shear components of the strain tensor lead to a nonuniform piezoelectric field⁴⁷, which is calculated taking into account up to second-order terms in strain. Next, electron and hole (time-reversed valence-band electron) eigenstates are calculated using a numerical implementation⁴⁸ of the eight-band envelope-function $k\cdot p$ theory^{49,50} including the calculated strain and piezoelectric fields as well as spin-orbit effects (for the explicit form of the Hamiltonian and details of numerical implementation, see Ref. ⁵¹; for material parameters used for the InAs/InP material system see Ref. ⁴² and references therein). Calculated eigenstates have the form of discretized envelope functions for each of the eight bands included in the model, which allows us to determine, e.g., the light-hole admixture to the hole ground state. For each of simulated QDs a 40×40 electron-hole single-particle basis is computed and used to calculate the eigenstates of excitons, charged excitons and biexcitons within the configuration-interaction method by exact diagonalization of the electron-hole Coulomb and phenomenological anisotropic exchange interactions expanded in the configuration basis. Finally, using the light-matter coupling Hamiltonian in the dipole approximation⁵², optical transition dipole moments and resultant radiative lifetime and degree of polarization are calculated for each of the carrier-complex states.

Acknowledgements

We acknowledge support from the Danish National Research Foundation via Research Centre of Excellence NanoPhoton (ref. DNRF147). P. H. was funded by the Polish National Science Center within the Etiuda 8 scholarship (Grant No. 2020/36/T/ST5/00511) and by the European Union under the European Social Fund. We are grateful to Krzysztof Gawarecki for sharing his implementation of the $k\cdot p$ method. Numerical calculations have been carried out using resources provided by Wroclaw Centre for Networking and Supercomputing (<https://wcss.pl>).

References

1. Senellart, P., Solomon, G. S. & White, A. High-performance semiconductor quantum-dot single-photon sources. *Nat. Nanotechnol.* **12**, 1026–1039 (2017).
2. Schweickert, L. *et al.* On-demand generation of background-free single photons from a solid-state source. *Appl. Phys. Lett.* **112**, 093106 (2018).
3. Basso Basset, F. *et al.* Quantum key distribution with entangled photons generated on demand by a quantum dot. *Sci. Adv.* **7**, eabe6379 (2021).
4. Aharonovich, I., Englund, D. & Toth, M. Solid-state single-photon emitters. *Nat. Photonics* **10**, 631–641 (2016).
5. Wang, Z. M. *et al.* Towards optimal single-photon sources from polarized microcavities. *Nat. Photonics* **13**, 770–775 (2019).
6. Wehner, S., Elkouss, D. & Hanson, R. Quantum internet: A vision for the road ahead. *Science (80-.)*. **362**, eaam9288 (2018).

7. Hepp, S., Jetter, M., Portalupi, S. L. & Michler, P. Semiconductor Quantum Dots for Integrated Quantum Photonics. *Adv. Quantum Technol.* **2**, 1900020 (2019).
8. Semenova, E. *et al.* Metamorphic approach to single quantum dot emission at 1.55 μm on GaAs substrate. *J. Appl. Phys.* **103**, 103533 (2008).
9. Paul, M. *et al.* Single-photon emission at 1.55 μm from MOVPE-grown InAs quantum dots on InGaAs/GaAs metamorphic buffers. *Appl. Phys. Lett.* **111**, 033102 (2017).
10. Nawrath, C. *et al.* Coherence and indistinguishability of highly pure single photons from non-resonantly and resonantly excited telecom C-band quantum dots. *Appl. Phys. Lett.* **115**, 023103 (2019).
11. Zeuner, K. D. *et al.* On-demand generation of entangled photon pairs in the telecom C-band for fiber-based quantum networks. 1–10 (2019).
12. Miyazawa, T. *et al.* Single-photon emission at 1.5 μm from an InAs/InP quantum dot with highly suppressed multi-photon emission probabilities. *Appl. Phys. Lett.* **109**, 132106 (2016).
13. Skiba-Szymanska, J. *et al.* Universal Growth Scheme for Quantum Dots with Low Fine-Structure Splitting at Various Emission Wavelengths. *Phys. Rev. Appl.* **8**, 014013 (2017).
14. Ha, N. *et al.* Single photon emission from droplet epitaxial quantum dots in the standard telecom window around a wavelength of 1.55 μm . *Appl. Phys. Express* **13**, 025002 (2020).
15. Portalupi, S. L., Jetter, M. & Michler, P. InAs quantum dots grown on metamorphic buffers as non-classical light sources at telecom C-band: a review. *Semicond. Sci. Technol.* **34**, 053001 (2019).
16. Cao, X., Zopf, M., Ding, Y. & Ding, F. Telecom wavelength single photon sources. *J. Semicond.* **40**, 071901 (2019).
17. Arakawa, Y. & Holmes, M. J. Progress in quantum-dot single photon sources for quantum information technologies: A broad spectrum overview. *Appl. Phys. Rev.* **7**, 021309 (2020).
18. Anderson, M. *et al.* Coherence in single photon emission from droplet epitaxy and Stranski–Krastanov quantum dots in the telecom C-band. *Appl. Phys. Lett.* **118**, 014003 (2021).
19. Musiał, A. *et al.* High-Purity Triggered Single-Photon Emission from Symmetric Single InAs/InP Quantum Dots around the Telecom C-Band Window. *Adv. Quantum Technol.* **3**, 1900082 (2019).
20. Gurioli, M., Wang, Z. M., Rastelli, A., Kuroda, T. & Sanguinetti, S. Droplet epitaxy of semiconductor nanostructures for quantum photonic devices. *Nat. Mater.* **18**, 799–810 (2019).
21. Müller, T. *et al.* A quantum light-emitting diode for the standard telecom window around 1,550 nm. *Nat. Commun.* **9**, 862 (2018).
22. Kuroda, T. *et al.* Symmetric quantum dots as efficient sources of highly entangled photons: Violation of Bell’s inequality without spectral and temporal filtering. *Phys. Rev. B* **88**, 041306 (2013).
23. Juska, G., Dimastrodonato, V., Mereni, L. O., Gocalinska, A. & Pelucchi, E. Towards quantum-dot arrays of entangled photon emitters. *Nat. Photonics* **7**, 527–531 (2013).
24. Liu, X. *et al.* Vanishing fine-structure splittings in telecommunication-wavelength quantum

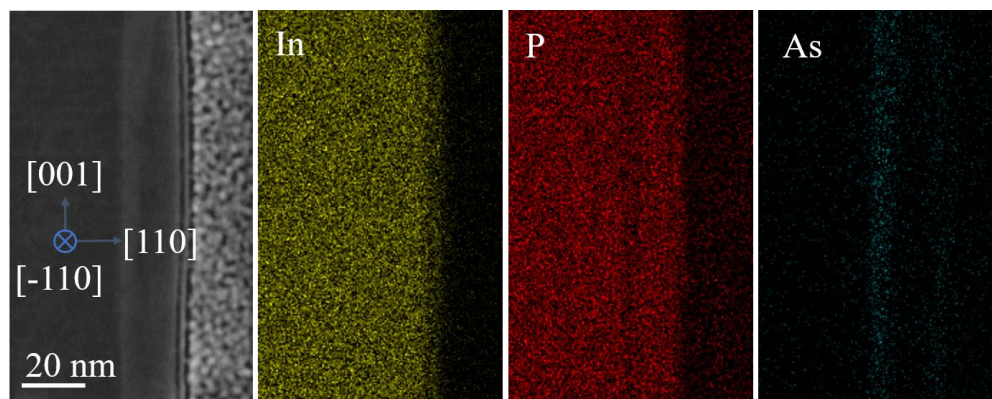
- dots grown on (111)A surfaces by droplet epitaxy. *Phys. Rev. B* **90**, 081301 (2014).
25. Ha, N. *et al.* Wavelength extension beyond 1.5 μm in symmetric InAs quantum dots grown on InP(111)A using droplet epitaxy. *Appl. Phys. Express* **9**, 101201 (2016).
 26. Schliwa, A., Winkelkemper, M., Lochmann, A., Stock, E. & Bimberg, D. In(Ga)As/GaAs quantum dots grown on a (111) surface as ideal sources of entangled photon pairs. *Phys. Rev. B - Condens. Matter Mater. Phys.* **80**, (2009).
 27. Ranjbar Jahromi, I. *et al.* Optical properties and symmetry optimization of spectrally (excitonically) uniform site-controlled GaAs pyramidal quantum dots. *Appl. Phys. Lett.* **118**, 073103 (2021).
 28. Wang, Z. M., Holmes, K., Mazur, Y. I., Ramsey, K. A. & Salamo, G. J. Self-organization of quantum-dot pairs by high-temperature droplet epitaxy. *Nanoscale Res. Lett.* **1**, 57–61 (2006).
 29. Wang, Z. M., Liang, B. L., Sablon, K. A. & Salamo, G. J. Nanoholes fabricated by self-assembled gallium nanodrive on GaAs(100). *Appl. Phys. Lett.* **90**, 113120 (2007).
 30. Huo, Y. H., Rastelli, A. & Schmidt, O. G. Ultra-small excitonic fine structure splitting in highly symmetric quantum dots on GaAs (001) substrate. *Appl. Phys. Lett.* **102**, 152105 (2013).
 31. Heyn, C. *et al.* Highly uniform and strain-free GaAs quantum dots fabricated by filling of self-assembled nanoholes. *Appl. Phys. Lett.* **94**, 183113 (2009).
 32. Sala, E. M., Na, Y. I., Godsland, M., Trapalis, A. & Heffernan, J. InAs/InP Quantum Dots in Etched Pits by Droplet Epitaxy in Metalorganic Vapor Phase Epitaxy. *Phys. Status Solidi - Rapid Res. Lett.* **14**, 1–6 (2020).
 33. Kadkhodazadeh, S. High resolution STEM of quantum dots and quantum wires. *Micron* **44**, 75–92 (2013).
 34. González, M. U. *et al.* In situ measurements of As/P exchange during InAs/InP(0 0 1) quantum wires growth. *Appl. Surf. Sci.* **188**, 188–192 (2002).
 35. Carlsson, N. *et al.* Growth of self-assembled InAs and InAs_xP_{1-x} dots on InP by metalorganic vapour phase epitaxy. *J. Cryst. Growth* **191**, 347–356 (1998).
 36. Osipov, A. V., Schmitt, F., Kukushkin, S. A. & Hess, P. Stress-driven nucleation of coherent islands: Theory and experiment. *Appl. Surf. Sci.* **188**, 156–162 (2002).
 37. Dubrovskii, G., Cirilin, E. & Ustinov, M. Kinetics of the initial stage of coherent island formation in heteroepitaxial systems. *Phys. Rev. B - Condens. Matter Mater. Phys.* **68**, 1–9 (2003).
 38. Abbarchi, M. *et al.* Poissonian statistics of excitonic complexes in quantum dots. *J. Appl. Phys.* **106**, 053504 (2009).
 39. Baier, M. H., Malko, A., Pelucchi, E., Oberli, D. Y. & Kapon, E. Quantum-dot exciton dynamics probed by photon-correlation spectroscopy. *Phys. Rev. B* **73**, 205321 (2006).
 40. Tsitsishvili, E. Impact of heavy hole–light hole coupling on the exciton fine structure in quantum dots. *Phys. E Low-Dimensional Syst. Nanostructures* **87**, 161–165 (2017).
 41. Musiał, A. *et al.* Plug&Play Fiber-Coupled 73 kHz Single-Photon Source Operating in

- the Telecom O-Band. *Adv. Quantum Technol.* **3**, 2000018 (2020).
42. Holewa, P. *et al.* Optical and electronic properties of low-density InAs/InP quantum-dot-like structures designed for single-photon emitters at telecom wavelengths. *Phys. Rev. B* **101**, 195304 (2020).
 43. Dusanowski, Ł. *et al.* Single-photon emission of InAs/InP quantum dashes at 1.55 μm and temperatures up to 80 K. *Appl. Phys. Lett.* **108**, 163108 (2016).
 44. Michler, P. *et al.* Quantum correlation among photons from a single quantum dot at room temperature. *Nature* **406**, 968–970 (2000).
 45. Dusanowski, Ł. *et al.* Strongly temperature-dependent recombination kinetics of a negatively charged exciton in asymmetric quantum dots at 1.55 μm . *Appl. Phys. Lett.* **113**, 043103 (2018).
 46. Dusanowski, Ł. *et al.* Confinement regime in self-assembled InAs/InAlGaAs/InP quantum dashes determined from exciton and biexciton recombination kinetics. *Appl. Phys. Lett.* **111**, (2017).
 47. Caro, M. A., Schulz, S. & O'Reilly, E. P. Origin of nonlinear piezoelectricity in III-V semiconductors: Internal strain and bond ionicity from hybrid-functional density functional theory. *Phys. Rev. B - Condens. Matter Mater. Phys.* **91**, 1–9 (2015).
 48. Gawarecki, K., Machnikowski, P. & Kuhn, T. Electron states in a double quantum dot with broken axial symmetry. *Phys. Rev. B - Condens. Matter Mater. Phys.* **90**, 1–8 (2014).
 49. Burt, M. G. The justification for applying the effective-mass approximation to microstructures. *J. Phys. Condens. Matter* **4**, 6651–6690 (1992).
 50. Foreman, B. A. Effective-mass Hamiltonian and boundary conditions for the valence bands of semiconductor microstructures. *Phys. Rev. B* **48**, 4964–4967 (1993).
 51. Gawarecki, K. Spin-orbit coupling and magnetic-field dependence of carrier states in a self-assembled quantum dot. *Phys. Rev. B* **97**, 1–9 (2018).
 52. Thränhardt, A., Ell, C., Khitrova, G. & Gibbs, H. M. Relation between dipole moment and radiative lifetime in interface fluctuation quantum dots. *Phys. Rev. B* **65**, 035327 (2002).

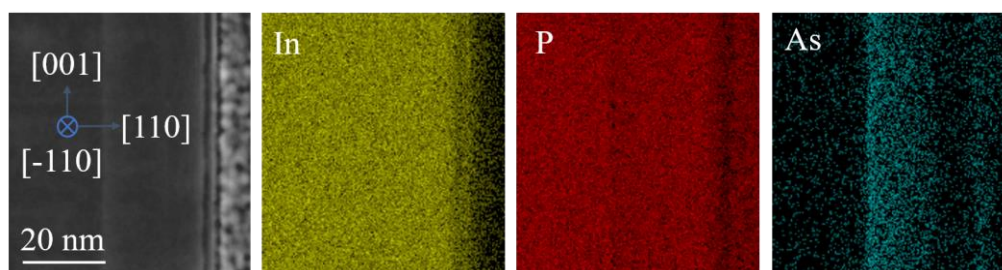
Supplemental Material

Section 1. EDX data

In this section we show the raw EDX data which form the basis for the EDX profiles plotted in Fig. 2(g) for the QD and Fig. 2(i) for the 2D layer.



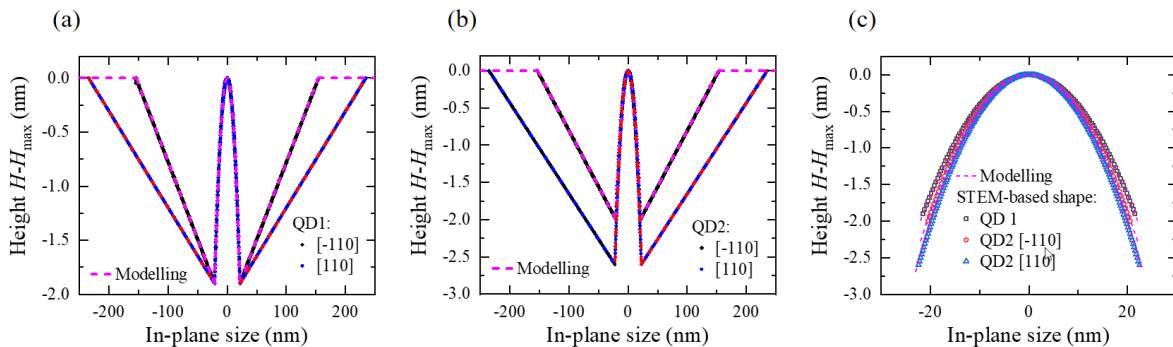
Supplementary Figure 1. EDX data for a QD viewed along the $[-110]$ direction.



Supplementary Figure 2. EDX data for the 2D layer viewed along the $[-110]$ direction.

Section 2. Results of the pit etching models.

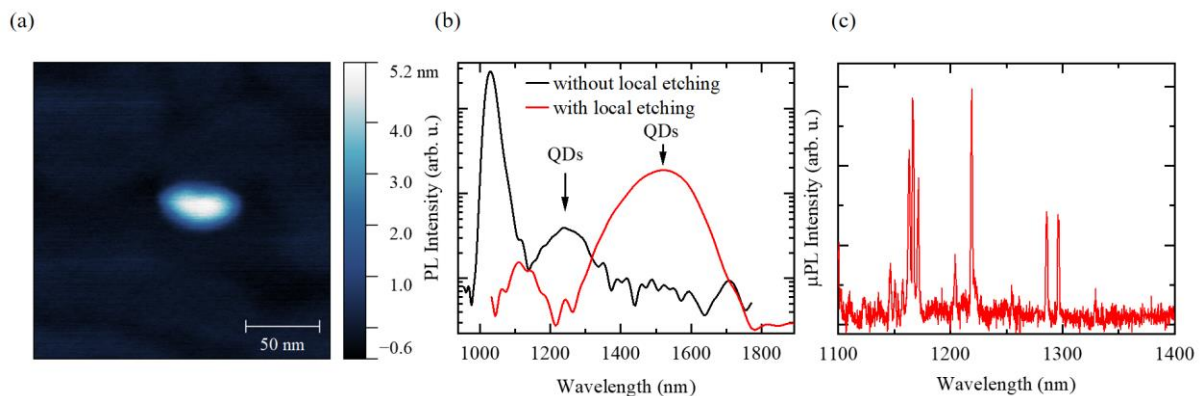
The results of QD-induced etching of InP are summarized in Supplementary Figure 3. Assumed geometry of the 2D layer is shown with the solid lines while the dashed lines show the results of the model, described in the text.



Supplementary Figure 3. Comparison of the assumed geometry of the pits and the 2D layer with the results of kinetic theory modelling for (a) the symmetric QD (QD1), (b) realistic QD with a slight asymmetry (QD2). (c) The close-up for the bottom of the QD.

Section 3. Comparison with the structure without annealing

Supplementary Figure 4 compares the optical spectra for the structure with and without applied annealing.



Supplementary Figure 4. (a) AFM image of a single QD for the structure without annealing. (b) Comparison of PL spectra for the structure with annealing (red solid line) and without annealing (black solid line). (c) μ PL spectrum for the structure without annealing.

The high asymmetry of the QDs without annealing, shown in the histogram in Fig. 1(e) is underline in high-resolution AFM image shown in panel (a) of Supplementary Figure 4. The cross-sections that correspond to that QD are shown in Fig. 1(d). The annealed QDs are found to red-shift the emission energy: the QD PL peak initially centered at ~ 1220 nm is shifted to ~ 1500 nm. As the density of QDs is largely unchanged by the annealing, we observe well-resolved single μ PL lines also from the structure without annealing, evidencing also its high structural quality.